



Shear and dilational interfacial rheology of surfactant-stabilized droplets [☆]

Kendra A. Erk ¹, Jeffrey D. Martin ², Jonathan T. Schwalbe ³, Frederick R. Phelan Jr., Steven D. Hudson ^{*}

Complex Fluids Group, Polymers Division, National Institute of Standards and Technology, 100 Bureau Drive, Gaithersburg, MD 20899, USA

ARTICLE INFO

Article history:

Received 12 January 2012

Accepted 27 March 2012

Available online 5 April 2012

Keywords:

Interfacial rheology

Rheology

Complex fluids

Emulsions

Droplets

Surfactant

Marangoni effects

Microfluidics

Particle tracking

ABSTRACT

A new measurement method is suggested that is capable of probing the shear and dilational interfacial rheological responses of small droplets, those of size comparable to real emulsion applications. Freely suspended aqueous droplets containing surfactant and non-surface-active tracer particles are transported through a rectangular microchannel by the plane Poiseuille flow of the continuous oil phase. Optical microscopy and high-speed imaging record the shape and internal circulation dynamics of the droplets. Measured circulation velocities are coupled with theoretical descriptions of the droplet dynamics in order to determine the viscous (Boussinesq) and elastic (Marangoni) interfacial effects. A new Marangoni-induced stagnation point is identified theoretically and observed experimentally. Particle velocimetry at only two points (including gradients) in the droplet is sufficient to determine the amplitudes of the dilational and shear responses. We investigate the sensitivity for measuring interfacial properties and compare results from droplets stabilized by a small-molecule surfactant (butanol) and those stabilized by relatively large block copolymer molecules. Future increased availability of shear and dilational interfacial rheological properties is anticipated to lead to improved rules of thumb for emulsion preparation, stabilization, and general practice.

Published by Elsevier Inc.

1. Introduction

Surfactants are added to fluids in order to modify interfacial properties: reduce interfacial tension, induce Marangoni elasticity, and introduce viscoelastic properties to the interface. Such changes have dramatic impact on emulsion properties. They make or break emulsion stability. Of these properties, interfacial rheology is the least studied, yet it is known to significantly retard droplet coalescence [1,2]. Improved measurement techniques for interfacial rheology should advance understanding of its effect on emulsion performance. Here we suggest a new interfacial rheology method that tests small droplets directly, those of size comparable to real emulsion applications.

Interfacial rheology [3] is challenging theoretically and experimentally; theoretically, the boundary conditions at the interface

are complex (including shape, motion, tension, and surfactant concentration) and unknown *a priori*. Experimentally, dilational and shear properties are both relevant, yet not readily accessible [4]. Generally, different techniques are required for each property: ring [5], needle [6,7], and bicone [8] geometries for shear; and pendant droplet, capillary wave, and Wilhelmy techniques for dilation [9,10].

To examine small droplets, microfluidic technology presents various advantages. Microfluidic devices offer rapid, steady droplet production, and multiple fluid inlets allow for high-throughput capability. Furthermore, the channel geometry can be altered easily to prescribe the desired flow. In past work, microfluidic devices similar to those employed here were used to measure the interfacial tension of multicomponent immiscible liquids [11] and probe mass transport and interfacial kinetics from droplets during a liquid-phase extraction process [12].

A suspended droplet in flow travels at a velocity that is intermediate to neighboring velocities in the surrounding fluid, thus causing the droplet fluid to circulate. Due to the spherical nature of droplets, the natural language for their internal circulation and interfacial dynamics is vector spherical harmonics, which importantly form two types: an area element on the surface of the sphere deforms either with or without changing area. Dilational types of course involve contraction or expansion of an area element, whereas shear types involve only a change in shape. By flowing droplets through a microchannel, we excite behavior of

[☆] Official contribution of the National Institute of Standards and Technology; not subject to copyright in the United States.

^{*} Corresponding author.

E-mail address: steven.hudson@nist.gov (S.D. Hudson).

¹ Present address: School of Materials Engineering, Purdue University, West Lafayette, IN 47907, USA.

² Present address: Johnson & Johnson Consumer & Personal Products Worldwide, Skillman, NJ 08558, USA.

³ Present address: MITRE Corporation, McLean, VA 22102, USA.

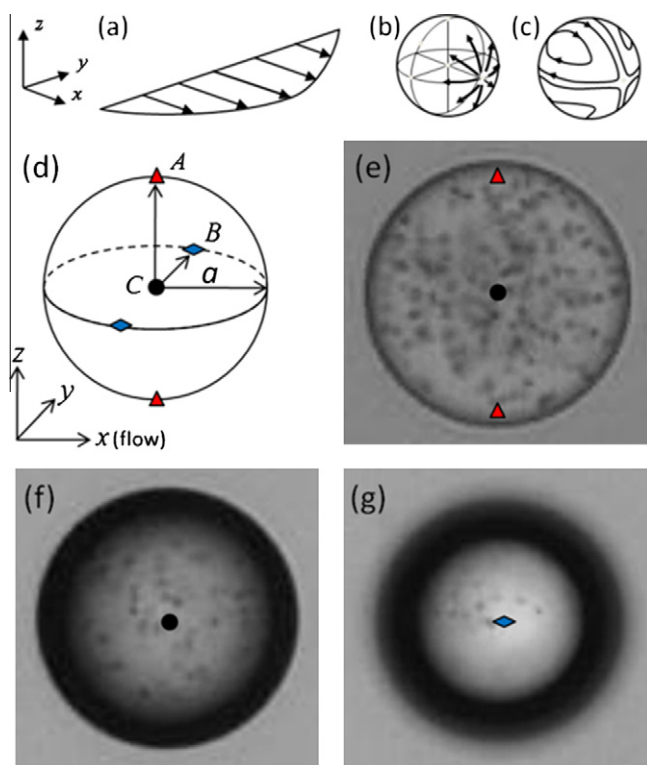


Fig. 1. Experimental geometry to measure the internal circulation of a droplet (radius, a) by particle velocimetry. (a) A plane Poiseuille flow (with velocity along x and velocity gradient along y) is set up within a rectangular microchannel. A droplet in the center of this flow samples different flow rates in its surroundings, and internal circulation patterns are established. These are (b) dilational (area-compressible), where fluid in the center of the droplet advances to the leading nose and returns to the rear about the periphery, and (c) shear (area-incompressible), where the interface experiences only shear and the fluid in the center is motionless (illustrated schematically here in the droplet frame of reference). (d) Velocimetry is carried out primarily at three points: A–C. The viewpoint for the following images is in the y -direction. (e) Image of the x – z mid-plane ($y = 0$) of a water/ethylene glycol droplet ($a = 49 \mu\text{m}$) in silicone oil, an “index-matched” system. (f) Image of the x – z mid-plane ($y = 0$) of a water droplet ($a = 52 \mu\text{m}$) in mineral oil. (g) Image of the x – z plane at the top ($y = -a$) of the water droplet in mineral oil. Note that the droplet edge in (g) is out of focus.

each type (shown schematically in Fig. 1b and c), and their magnitudes directly indicate the respective dilational and shear properties of the interface. For a droplet on the centerline of plane Poiseuille flow (illustrated in Fig. 1a), the circulation relative to the droplet center is a type of fountain flow. Theoretical analysis, described in our recent article [13], concludes that velocimetry at only two points in the droplet is sufficient to determine the amplitudes of the dilational and shear behavior. (A similar analysis of vesicular spherical caps in flow attached to a solid surface also points to this method of measuring interfacial viscosity [14,15].) In this paper, we explore Marangoni effects and demonstrate theoretically that they too can be determined by measuring the velocity gradient at one of these points. We carry out such measurements and compare to new theoretical predictions.

2. Experimental methods

To accomplish these measurements, optical microscopy and high-speed imaging record the shape and internal circulation dynamics of droplets in plane Poiseuille flow through a rectangular microfluidic channel.

2.1. Materials

In this study, solutions of ethylene glycol (from J.T. Baker⁴) and distilled water containing various concentrations of surfactant were prepared for use as the droplet phase; silicone oil (Gelest T22) was used as the continuous phase. The ethylene glycol/water mixtures were prepared in either a 40/60 or a 50/50 mass ratio to achieve a desired refractive index contrast to the silicone oil phase. Two surfactants were investigated: a small-molecule alcohol surfactant – *n*-butanol (Mallinckrodt) at (0.70, 1.7, 3.4, and 6.8)% mass fraction; a diblock copolymer surfactant – poly(dimethyl siloxane-*b*-ethylene oxide) at (0.1 and 1.0) mmol/L concentrations (Polysciences, Inc., 3000 g/mol, 80% mass fraction ethylene oxide). Polystyrene spheres (2 μm diameter, Polysciences, Inc.) were added to the droplet phase in concentrations less than 0.2% mass fraction to serve as tracer particles for the velocimetry measurements. All materials were used as received. The viscosities of the oil and aqueous phases are approximately (200 and 2) mPa s at 23 °C, respectively.

Consistent with these surfactants, we assume that the interface is always fluid. Therefore, our theoretical analysis does not consider solid or viscoelastic material at the interface. At a high enough rate, polymeric surfactants may eventually be viscoelastic, but here the interfacial deformation rates are less than 10 s^{-1} , as noted below.

2.2. Microchannel design

Microfluidic channels were fabricated using soft lithography and poly(dimethylsiloxane) replication as described elsewhere [11,12,16,17]. Microfluidic devices were mounted on an Olympus IX71 inverted microscope fitted with an automated translating XY stage (Prior H107). Fluid was driven by microstepping syringe pumps (New Era), capable of delivering fluid with accuracy better than 0.1%. Aqueous droplets were formed at a *T*-junction and promptly enter the microfluidic channel. There are two inlets for the aqueous phase and several inlets for the oil phase, allowing for control of the droplet position (in three dimensions) and speed in the channel [12]. Because of small variations in the microchannel geometry during fabrication, each microfluidic device formed droplets at different vertical heights in the channel. In order to minimize the difference (y_0) in the position of the droplet mid-plane and the centerline of the channel, precise control of the droplet height was achieved through the injection or withdrawal of continuous phase fluid from an inlet positioned above the microchannel and downstream from the droplet formation zone [12]. This height adjustment was made in order to produce images similar to Fig. 1e and f, in which the microscope is focused on the mid-plane of the channel.

2.3. Interfacial tension measurements

Each experiment involves recording the age, shape, and internal circulation of droplets as they convey near the centerline of a rectangular microfluidic channel. The microchannels used in this study had typical dimensions of 1500 μm width by 300 μm height in the wide portion of the channel, giving an aspect ratio of 5. The channel featured multiple 5:1:5 constriction/expansion zones that facilitated the measurement of the liquid–liquid interfacial tension. Upon entering the constriction, the fluid accelerated and an extensional flow was present on the centerline of the channel. This

⁴ Certain commercial materials and equipment are identified in this paper in order to adequately specify the experimental procedure. In no case does such identification imply recommendation or endorsement by the National Institute of Standards and Technology, nor does it imply that these are necessarily the best available for the purpose.

extensional flow acted to distort the droplet. By balancing this (known) force with the interfacial restoring force, the interfacial tension can be determined simply by measuring the droplet shape and its position as a function of time as described in detail previously [11,12,18]. This acceleration occurs during a period typically of approximately 30 ms. This is very short compared to the age of the interface (typically seconds). As we illustrate in later calculations, flow may cause gradients in interfacial tension. Such gradients are small here and have negligible effect on the ellipsoidal deformation measured here to evaluate interfacial tension. Instead, those gradients should induce higher-order deformation modes (viz., 4th order), which have not been evaluated here. In context then, these interfacial tension measurements approximate the instantaneous average value over the surface of the drop.

A custom-built LabVIEW routine utilized a high-speed camera (Redlake HG100-k, with 12 μm pixel size) to automatically track the droplets and their deformation while entering a constriction. The interfacial tension was calculated based on analysis of the acquired images (8-bit grayscale, 1504 \times 400 pixels). The constrictions were placed in varying positions along the channel, allowing for dynamic time-point measurement of the interfacial tension as a function of interface age. The range of interface age accessible in the current devices was approximately (0.5–20) s. A more detailed description of the data acquisition, analysis, and interfacial tension calculation can be found elsewhere.[12]

2.4. Internal circulation measurements

Fluid circulation inside the droplets is revealed through the use of micron-sized tracer particles. For particle velocimetry, a series of high-speed images were captured (typically a few hundred), and from those images, an individual series of (smaller) images of each analyzed droplet were extracted. These individual images were extracted based on the droplet's center of mass, yielding a series of images of the droplet flowing down the channel that are in the reference frame of the droplet. The position of the tracer particles was tracked with time as the droplet flowed through the wide portion of the channel just prior to the constrictions such that the observed circulation profiles can then be correlated with the measured interfacial tension. The x -component of the circulation velocity, $v_x(i)$, is measured in the reference frame of the droplet at any point i in the droplet and non-dimensionalized by the droplet velocity v_d in the laboratory frame and scaled by $(2a/h)^2$, where a is the droplet radius and h is the microchannel height.

The heights (i.e., positions along the optic axis) of the droplets, tracer particles, and bounding walls of the channel were determined using microscope focus. At a given focus setting, the depth of field is given by [19,20]

$$d = \frac{\lambda_{hv} \sqrt{n^2 - NA^2}}{NA^2} + \frac{p}{MNA}, \quad (1)$$

where λ_{hv} (550 nm) is the wavelength of light, n (1) is the refractive index between the lens and object, NA (0.40) is the numerical aperture, p (12 μm) is the pixel size on the chip, and M (32 \times) is the magnification. Given these parameters, $d = 4.1 \mu\text{m}$, that is, objects within $\pm 2.0 \mu\text{m}$ are generally considered to be in focus. Tracer particles within this depth appear dark, since they scatter light strongly. The position of other objects can be identified with slightly greater precision, since their image changes qualitatively at focus. Specifically, for an object in the depth of field, it is surrounded by a fine fringe that is either dark or bright, whether it is above or below the focal plane. Nevertheless, finite depth of field causes uncertainty in the observation position and thus of the viscosity measurements based on it.

In our experiments, it was convenient to measure the circulation velocity of the droplet's fluid at two locations on the mid-plane of the droplet ($y = 0$): at the center of the droplet (point C in Fig. 1d) and the edge of droplet (points A or B in Fig. 1d). As discussed in the next section, we chose these locations for our velocimetry measurements because the effects of dilation and shear are separable at these locations and the velocity at point C depends on dilation only and not on shear when the droplet is flowing on the channel centerline.

The location A or B chosen for velocimetry depended on the optical characteristics of the droplet and continuous phases. This is illustrated in Fig. 1e–g. By design, the ethylene glycol/water droplet had a refractive index similar to the silicone oil continuous phase, allowing for visualization of the tracer particles near the droplet interface (see Fig. 1e). In this nearly “index-matched” case, velocimetry at the droplet center (at point C, ●) and edge (at two A points, ▲) can be performed by capturing a single image sequence of the mid-plane of the droplet as it travels down the channel.

However, many systems of interest may have substantially different indices of refraction. For example, in a pure water droplet in mineral oil, the tracer particles at the droplet's mid-plane near the interface cannot be resolved (see Fig. 1f). Once again, we want to measure velocities at both the interface and the interior in order to sample the dilation and shear interfacial effects. Velocimetry must thus be performed on image sequences captured at different planes of focus: the velocity at the droplet's center is obtained from images captured at the mid-plane ($y = 0$; point C in Fig. 1f), whereas the velocity at the droplet's edge is obtained from images of the B regions of the droplet (e.g., Fig. 1g). These B regions at $y = \pm a$ experience equivalent forces when the droplet is flowing on the channel centerline. Differences in velocity at $y = \pm a$ would thus suggest that the droplet is not on the centerline, that is, y_0 is finite (see Appendix A).

3. Theory

Ultimately, we are interested in relating the internal circulation measurements to the interfacial rheology of the system and investigating how the circulation and rheology changes with surfactant concentration.

3.1. Viscous interfacial effects

Recently [13], we found that if the interface may be described as purely viscous, particle velocimetry at only two points in the droplet is sufficient to determine the magnitudes of the dilational and shear Boussinesq numbers, Bq^d and Bq^s , which are measures of the relative strength of the interfacial viscous forces to the bulk viscous forces acting from the continuous phase at a fluid interface:

$$Bq^s = \frac{\mu^s}{\eta a}, \quad Bq^d = \frac{\kappa^s}{\eta a}, \quad (2)$$

where μ^s is the surface (interfacial) shear viscosity, κ^s is the surface (interfacial) dilational viscosity, a is the droplet radius, and η is the viscosity of the continuous fluid phase (200 mPa s for silicone oil).

As described in detail elsewhere [13], analytic solutions for the flow patterns within the viscous droplets are attainable under the assumptions that the droplet remains spherical, and Stokes flow conditions are assumed for the bulk fluids. The solution to the Stokes equations about a sphere is given in terms of vector spherical harmonics, and a plane unbounded Poiseuille flow is used to force the system. Adopting the Boussinesq–Scriven constitutive law for a viscous Newtonian interface, expressions for the slip velocity and velocity components at locations on and within the

droplet are found as a function of viscosity contrast and shear and dilational Boussinesq number (Eqs. (3) and (4) below).

The magnitude of the dilational Boussinesq number can be found by measuring the velocity of the fluid at the center of the droplet (i.e., point C):

$$v_x(C)^0 = \frac{1}{(2 + 2Bq^d + 3\lambda)}, \quad (3)$$

where λ is the viscosity ratio of the droplet phase to the continuous phase. The superscript 0 signifies that the interface is purely viscous, that is, without Marangoni effects.

To determine the shear Boussinesq number, the velocity may be measured at either the A or B point

$$v_x(A)^0 = \frac{5}{3(4+4Bq^d+\lambda)} - \frac{1}{2+2Bq^d+3\lambda} + \frac{7}{12v}, \quad (4)$$

$$v_x(B)^0 = -\frac{5}{3(4+4Bq^d+\lambda)} - \frac{1}{2+2Bq^d+3\lambda} - \frac{7}{3v},$$

where $v = 7(1 + \lambda) + 12Bq^d + 10Bq^s$. These equations are then solved for Bq^s [13]:

$$Bq^s = \frac{5}{(16v_x(A)^0 + 4v_x(B)^0 + 20v_x(C)^0)} - \frac{\lambda}{4} - 1. \quad (5)$$

When Bq^d is very large, $v_x(C)^0$ is zero and Eq. (4) states that $v_x(A)^0$ and $v_x(B)^0$ are equal and opposite. From spherical harmonic analysis, it is known that $v_x(C)^0$ is proportional to the (compressible) dilational modes of circulation in the droplet, consistent with Eq. (3), and $v_x(A)^0$ and $v_x(B)^0$ depend also on the (area-incompressible) shear modes [13]. Schematics of these two circulation modes are illustrated in Fig. 1b and c. The area-incompressible mode (Fig. 1c) comprises vortices that intersect the center of the droplet. When the modes are added together, these vortices intersect only the y-axis, and the position of these stagnations along y depends on Bq^d and Bq^s [13]. These modes remain symmetric front to back (i.e., $\pm x$), as long as Marangoni effects are absent.

3.2. Elastic interfacial Marangoni effects

In addition to viscous effects at the interface, elastic effects are typically relevant, depending on the nature of the surfactant in the system. As described earlier [13], the same spherical harmonic approach was employed for dynamic interfacial rheology predictions at finite Marangoni number Ma and surface Peclet number Pe .

The Marangoni number Ma is the ratio between the dimensionless elasticity and capillary numbers, $Ma = E/Ca$, and it determines the magnitude of surfactant concentration gradients on the surface of the droplet. The elasticity number $E = (\partial\sigma/\partial\Gamma)\Gamma/\sigma$ measures the normalized sensitivity of interfacial tension σ to interfacial surfactant monolayer concentration Γ . A good approximation of E is typically Π/σ (Appendix B), where Π is the interfacial pressure ($\sigma_0 - \sigma$), the reduction in interfacial tension from the clean interface in the absence of any surfactant. Here we describe the variation of the surface tension as a linear perturbation about its equilibrium:

$$\sigma = \sigma_{eq} + Ma(\Gamma_{eq} - \Gamma)RT, \quad (6)$$

where the subscript eq denotes the uniform values of interfacial tension and concentration in equilibrium with the adjacent surroundings. $Ca = \eta v_0(2a/h)^2/\sigma$ is the capillary number, where v_0 is the (laboratory frame) flow velocity in the center of the channel and h is the channel depth (along y). Ca here ranges from 0.004 to 0.016. Surface tension nonlinearity is an issue only when gradients in interfacial concentration are relatively large, that is, at relatively large Ca and moderate to low Ma [21–23]. When Ma is sufficiently large, even modestly above 1 (see [21]), the gradients are small enough that the linear approximation is valid. That is, the interfacial

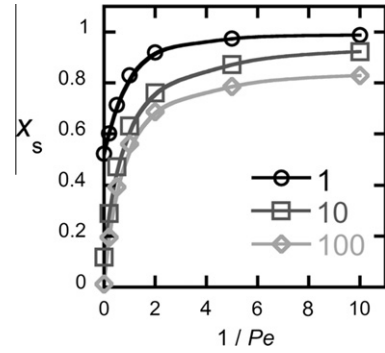


Fig. 2. Normalized stagnation point position (x_s) v. $1/Pe$, calculated when $Ma = 1, 10, 100$; $Bq^s = Bq^d = 0$. Lines are included to guide the eye.

tension may strongly disobey the 2D ideal gas law, but deviations are small enough to be described entirely by Eq. (6).

The Peclet number Pe is the ratio of convective to surface diffusive mass transport. Diffusive transport of course acts to dissipate the surfactant concentration gradients. Other mass transport processes may also act in parallel through the bulk. Although such processes are not modeled here directly, a qualitative understanding of the effects of mass transfer is assumed from surface diffusion, which is a surrogate for these other mechanisms as well, as discussed in more detail below. The surfactant evolution equation

$$\frac{\partial\Gamma}{\partial t} + \nabla \cdot (\mathbf{v}\Gamma) + \Gamma(\mathbf{v} \cdot \hat{\mathbf{n}})\nabla \cdot \hat{\mathbf{n}} - \frac{\nabla^2\Gamma}{Pe} = 0, \quad (7)$$

was integrated numerically (as described previously [13] using Mathematica, Wolfram Research) for Ma ranged from 0 to 300 and Pe from 10^{-4} to infinity, as appropriate for the two surfactant systems studied here. Detailed calculations are being reported in another publication; here we report some essential characteristics caused by Marangoni effects and the results that are most relevant to the experimental data.

As insinuated in the previous section, Marangoni effects induce fore-aft asymmetry of several manifestations. The first form of asymmetry is in surfactant concentration Γ and thus of σ . This asymmetry further induces fore-aft asymmetry of droplet circulation. Most significant here is the introduction of another stagnation point within the droplet, which lies on the x-axis and toward the rear of the droplet, and at the same time, the two stagnation points noted previously are shifted slightly toward the nose. The location of the stagnation point along the x-axis is quantified by x_s , the normalized deviation of the stagnation point from the center of the droplet. As seen in Fig. 2, the Marangoni-induced stagnation point is near to point C (i.e., droplet center, such that $x_s \approx 0$) when both Ma and Pe are large; the stagnation point approaches the tail of the droplet when either is small (such that $x_s \rightarrow 1$). The position x_s is influenced only very weakly by Bq^d and Bq^s . These viscosities significantly affect the magnitude of internal circulation, and Bq^d significantly influences the fore-aft asymmetry of Γ , but the influence of interfacial viscosity on fore-aft asymmetry of the circulation pattern is negligible. To determine the magnitude of Marangoni effects independent of interfacial viscosity, it is necessary to quantify this asymmetry. In principle, the velocity at any point along the x-axis may be adequate and need not be the point x_s where the velocity is zero. Equivalently, the flow gradient $\partial v/\partial x$ may be measured at the origin.

Marangoni elasticity also reduces the circulation velocity at the center of the droplet. Detailed results will be described elsewhere. When Ma and Pe are sufficiently large, the velocity at the droplet center approaches zero, as expected when dilational modes are arrested. Marangoni effects do not influence interfacial shear circula-

tion modes significantly, particularly when Ma is greater than 10, and thus Eq. (5) remains valid, even when the superscript 0 is dropped.

4. Experimental results and discussion

Two surfactant-stabilized systems were investigated in this study. We will first discuss the droplets stabilized by adsorption of diblock copolymer (bcp) molecules to the droplet/oil interface. Droplets stabilized by the small-molecule alcohol surfactant (butanol) showed more complex behavior and will be discussed afterward.

The main experimental objective is to measure interfacial rheology as a function of interfacial composition. We use interfacial tension here to indicate the interfacial composition. Since the concentrations of surfactant adjacent to the interface are quasi-equilibrated by kinetic sorption processes, the interfacial tension measured at a given interface age is a useful measure of the instantaneous average surfactant concentration adjacent to the interface.

4.1. Rheology of bcp-stabilized droplets

Nearly index-matched, aqueous droplets (40% mass fraction ethylene glycol) containing (0–1.0) mmol/L concentrations of PDMS-EO diblock copolymer (bcp) were investigated in the microchannel apparatus. The interfacial tension of the droplets was recorded as a function of time as the droplets flowed down the length of the microchannel (Fig. S1). Over a 12 s experimental observation window, the interfacial tension decreased at short times before reaching an approximate plateau at longer times, that is, as the interface aged and bcp adsorption occurred. Greater concentrations of bcp resulted in reduced values of interfacial tension. This behavior is consistent with the energetically favorable expectation of adsorption of the bcp at the aqueous droplet/oil interface: thermodynamics dictate that the ethylene oxide blocks remain in the aqueous phase while the PDMS blocks insert into the silicone oil phase, leading to a stable reduction in interfacial tension.

The circulation velocities measured at the edge and center of the droplets, $v_x(A)$ and $v_x(C)$ respectively, are displayed in Fig. 3 as a function of the corresponding interfacial tension of the droplet. In essence, Fig. 3 shows that the dilational deformation behavior is arrested for the bcp-stabilized droplet ($v_x(C)$ is near zero for the bcp-containing droplets) and circulation is dominated by the shear deformation type only. Negative velocities indicate motion of the

tracer particles in the $-x$ direction (in the reference frame of the droplet). Such behavior is most likely driven by the close proximity of a stagnation point, thought to be near the center of the droplet. For each data point, the reported velocity is an average of at least three separate velocity measurements from at least three different droplets; error bars represent one standard deviation of the multiple measurements. The spread in the measurements at each bcp concentration most likely results from a finite value of y_0 for some droplets, that is, slight deviation of some droplets from the centerline of the flow.

As seen in Fig. 3, $v_x(A)$ depended only weakly on interfacial tension (i.e., bcp concentration), and thus, the average velocity over all values of the interfacial tension can be determined for each bcp concentration and used to estimate the interfacial shear viscosity (see Table 1). From the values of Bq^s in Table 1, we see that there was no significant change observed in the interfacial shear viscosity of the droplets from the addition of bcp (except perhaps at 1 mmol/L).

As noted above, the small values of $v_x(C)$ observed in Fig. 3 indicate that interfacial dilation is largely arrested. Dilation can be arrested by either substantial Bq^d or Ma and Pe (discussed qualitatively above), that is, either viscous or elastic effects. If arrested by interfacial viscosity alone, then Bq^d ranges from approximately 15–50 (calculated from Eq. (3)), that is, much greater than Bq^s . Although dilational and shear interfacial viscosities have not been measured yet for bcp surfactants, previous measurements with small-molecule surfactants indicated that Bq^d was never orders of magnitude greater than Bq^s [24,25], and we suppose that it is not the case here either. Therefore, Marangoni suppression of dilation is here very plausible. Specifically, Ma is very large when bcp is present (Table 1; estimated $O(100)$). Even modest values of $Pe(O(1))$ are thus sufficient to suppress dilation.

Dilation is also suppressed even when the nominal surfactant concentration is zero. Marangoni effects are implicated again, because a sizeable interfacial pressure remains. Specifically, from pendant droplet tensiometry, the presence of tracer particles in a 40% mass fraction ethylene glycol/water droplet in the same oil leads to a reduction in interfacial tension from (30.5 ± 0.4) mN/m to (30.0 ± 0.1) mN/m for a system with tracer particles. A residual surface-active impurity thus accompanies the PS tracer particle solution. Ma therefore remains considerable (60) and able to largely suppress dilation. Similar interfacial pressure and Marangoni effects are present when the concentration of ethylene glycol is 50% mass fraction.

4.2. Rheology of butanol-stabilized droplets

Index-matched, aqueous droplets (50% mass fraction ethylene glycol) initially containing (0–6.8)% mass fraction butanol were investigated in the microchannel apparatus. The interfacial tension of the droplets as a function of time displayed more complex behavior than the bcp-containing droplets (see Fig. S2). Immedi-

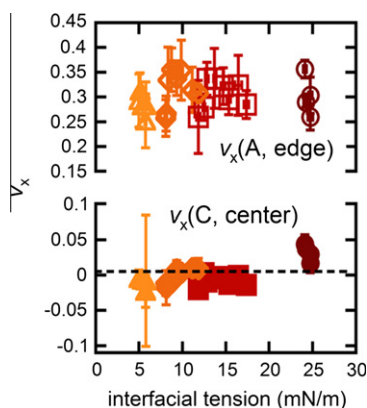


Fig. 3. Velicimetry data for bcp-stabilized aqueous droplets in silicone oil; open symbols indicate $v_x(A)$, and closed symbols indicate $v_x(C)$. The concentration of bcp in the droplet is varied: 0 mmol/L (●, ○), 0.05 mmol/L (■, □), 0.1 mmol/L (closed/open 'diamond'), and 1 mmol/L (closed/open 'triangle'). Error bars represent one standard deviation of the multiple measurements.

Table 1

Measured velocity and calculated shear Boussinesq numbers (Eq. (5)), interfacial shear viscosities (Eq. (2)), and Marangoni numbers for aqueous droplets containing a range of diblock copolymer concentrations. Reported values are (averages \pm one standard deviation) over the range of interfacial tensions observed at each bcp concentration.

Conc. bcp mmol/L	$v_x(A)$	Bq^s	$\mu^s (\times 10^{-6})$ Pa s m	Ma^a
0	0.302 ± 0.040	0.28 ± 0.19	2.7 ± 1.9	60
0.05	0.305 ± 0.029	0.33 ± 0.11	2.9 ± 1.0	200
0.1	0.318 ± 0.042	0.28 ± 0.17	2.5 ± 1.5	240
1.0	0.285 ± 0.025	0.45 ± 0.11	4.0 ± 1.0	280

^a Ma is calculated using the approximation $E = \Pi/\sigma$.

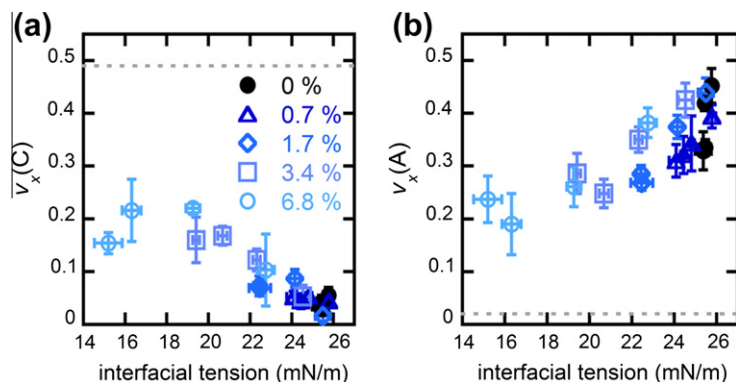


Fig. 4. Velocimetry measurements at the droplet's center (a) and edge (b) for (0–6.8)% mass fraction butanol-stabilized aqueous droplets in silicone oil. The velocities expected for a clean, fully mobile interface are indicated by the dotted line. Error bars indicate one standard deviation of repeated measurements.

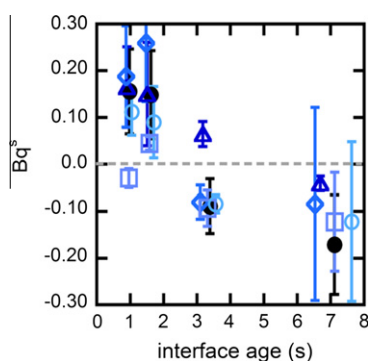


Fig. 5. Shear Boussinesq numbers for (0–6.8)% mass fraction butanol-stabilized aqueous droplets in silicone oil. However, at large age, the values determined for Bq^s are negative, a non-physical result. Symbols correspond to legend in Fig. 4a.

ately after the formation of the droplet, adsorption of the butanol to the interface occurred causing a rapid decrease in tension by the time of the first measurement, a more rapid response than observed with the larger and more dilute bcp molecules. And unlike the bcp, butanol is also soluble in the oil phase and is thus extracted from the droplet into the continuous phase. This extraction process, which continues as the droplet flows through the channel, caused an increase in interfacial tension with time [12], which was convenient for exploring transient effects within the time window accessible by the current approach.

The velocities measured at the center and edge of the butanol-stabilized droplets are displayed in Fig. 4 as a function of the interfacial tension of the droplet. For each point, the reported velocity is an average of at least three separate velocity measurements from at least three different droplets; error bars represent one standard deviation of the multiple measurements. When butanol is present, a range of circulation velocities are observed, depending strongly on the interfacial composition, with $v_x(C)$ and $v_x(A)$ increasing and decreasing, respectively, with increasing butanol concentration.

From the velocimetry results, Bq^s was calculated from Eq. (5); the results are displayed in Fig. 5 as a function of interface age. Bq^s is small and specifically smaller than the values observed for bcp-stabilized interfaces (reported in Table 1). Furthermore, Bq^s decreases during the butanol extraction process (i.e., as the droplet ages), suggesting that butanol removes the impurity from the interface as it desorbs. At longer interfacial age, Bq^s is essentially zero within experimental uncertainty. We assume that Bq^d is likewise small and also below our current sensitivity [24,25].

The relationship of mass transfer, Marangoni forces, and internal droplet circulation is illustrated further in Fig. 6 for droplets

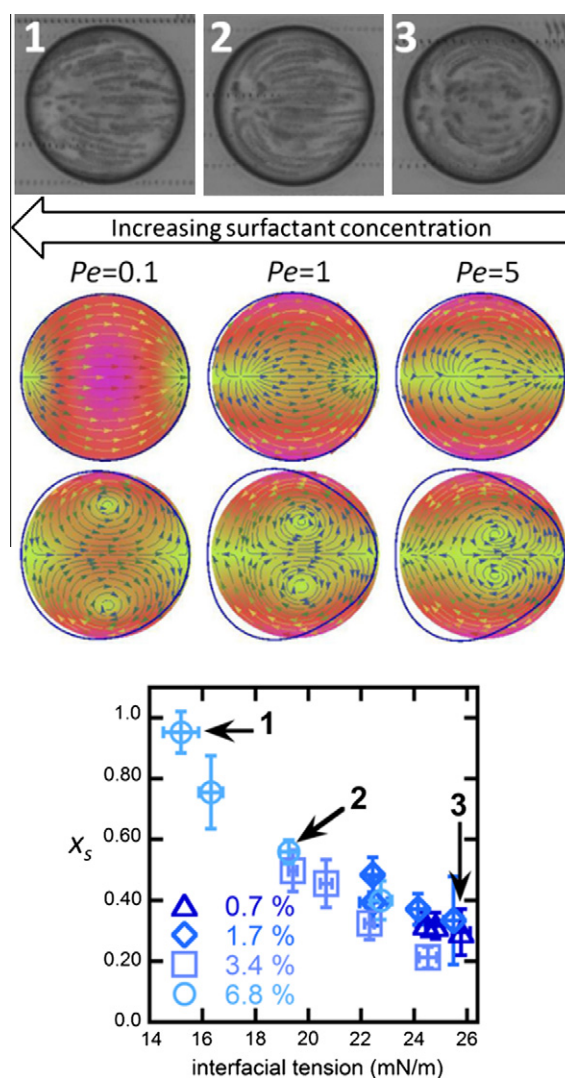


Fig. 6. Tracer particle streak images in the x–z mid-plane of a droplet (first row, $a = 45 \mu\text{m}$) and flow-field simulations in the x–z plane (second row) and x–y plane (third row) display the observed and theoretical circulation behavior of droplets containing increasing amounts of small-molecule surfactant (butanol) from right to left. Deviation of the stagnation point with respect to the droplet center is displayed as a plot of x_s v. interfacial tension. The simulated interfacial concentration of surfactant is represented by a closed loop, whose radius is $a(1 + 10\delta T/\Gamma_{eq})$, overlaid on the simulation snapshots in the second and third row; as the concentration of surfactant increases, the distribution of surfactant at the interface becomes increasingly uniform.

containing increasing concentrations of surfactant. The top row of Fig. 6 contains three particle streak images obtained experimentally from integrating approximately 100 frames of video sequence taken at a rate of 1000 Hz as the droplets convey through the wide segments of the microchannel (x - z plane). In each image, a stagnation point is observed along the horizontal x -axis; as introduced previously, the deviation of the stagnation point from the droplet's center is quantified by x_s and displayed graphically in Fig. 6 for the three different butanol concentrations (numbered data in the plot corresponds to numbered droplet images in top row of Fig. 6). The second row of Fig. 6 displays the corresponding theoretical streamlines in the x - z mid-plane of a droplet when $Ma = 10$ and Pe equals 0.1, 1, and 5; the third row illustrates sections in the orthogonal x - y plane of the droplet.

From Fig. 6, we observe that when mass transfer is very rapid (when surfactant concentration is high, *i.e.*, small effective Pe), the Marangoni-induced stagnation point is located near the droplet tail, which corresponds to x_s approaching unity. This stagnation point moves closer to the droplet center as the mass transfer rate slows down. The simulations, while reproducing the observed circulation patterns, are not meant to be an exact correspondence, nor to measure Ma or Pe , since experimentally mass transfer of surfactant is known to occur in the bulk [12], whereas the simulations consider the surfactant to be confined to the interface. The increase in mass transfer rate when surfactant concentration is high, and the corresponding increase in dilation rate (related to increasing $v_x(C)$ in Fig. 4a) has been observed and established previously; this behavior is called remobilization [26,27]. When surfactant concentration is high, rapid desorption at the droplet tail and adsorption at the nose cause the interfacial concentration to remain nearly uniform (as illustrated by the closed loops in Fig. 6) and thus permit dilational circulation to take place.

When surfactant is soluble in one of the phases, exchange of surfactant between the interface and the bulk occurs by transport to or from the interface and adsorption/desorption at the interface. In this circumstance, the ratio of interfacial to bulk concentrations (Γ/c) defines a length scale, which represents the distance through which surfactant mass transfer occurs. This length scale is important for evaluating characteristic time scales [28] and coalescence rates [29] in emulsions. In the present case, the appropriate length scale is larger because the butanol surfactant is not confined to one side of the interface. The amount adsorbed to the interface is no longer simply Γ but a characteristic flux through the interface. This difference must be considered for proper modeling of bulk mass transfer. In the absence of modeling, experiments such as those reported here remain useful comparisons.

5. Implications and future directions

As illustrated by the results displayed in Fig. 6, sorption rates can govern dilational flow rates, motivating future theoretical calculations that relate dilational droplet circulation velocities to bulk and interfacial surfactant mass transport properties and thereby establishing another method to determine interfacial sorption coefficients or diffusivities. A droplet-based approach for the measurements of these dynamics is of great interest, since the size of the droplet selects the prevailing mass transfer mechanisms.

Consistent with many surfactant-stabilized emulsions utilized in real-world applications, the interfacial viscosities investigated here are small and close to the limit of measurement sensitivity. To improve measurement precision, more accurate velocimetry is required. Currently, the particle position is determined by choosing the darkest pixel, and the spatial resolution is approximately the size of the particle, since this darkest pixel may be anywhere within the shadow of the particle. With these constraints, the current minimum measurable velocity is approximately $5 \mu\text{m/s}$. To achieve

greater accuracy, a different algorithm should be employed that would determine the particle position with sub-pixel accuracy using a particle shape fitting function [30]. Such approaches are better suited to fluorescence microscopy [31].

Another important improvement would be to explore a wider range of interfacial deformation rates. Interfacial deformation rates are approximately $(v_x(A) - v_x(B))v_o(2a/h)^2/2a$ for shear and $v_x(C)v_o(2a/h)^2/a$ for dilation. In the current bcp experiments, these are roughly 5 s^{-1} and 0.1 s^{-1} , respectively, deformation rates that are much slower compared to any molecular relaxation rates (*e.g.*, Rouse relaxation). Lower deformation rates are of particular interest for understanding emulsion and coalescence behavior. Much lower rates are not practical with the current flow-through approach utilizing small droplets. However, if flow is actuated pneumatically, instead of by means of syringe pumps, the flow rates can be adjusted much more rapidly and it is likely that small droplets may be produced at higher rates and then examined downstream at lower rates, or even with oscillatory forcing.

In the future, it is desirable to extend droplet-based measurements of interfacial rheological parameters to the study of viscoelastic membranes and vesicles. Such techniques would allow for these capsule-like bodies to be measured in a spherical geometry and on size scales that are similar to biological scales. Thus, interfacial rheological properties such as compressibility and membrane mobility could be studied in a more natural way without resorting to planar geometries or more invasive techniques such as capsule aspiration and optical tweezing. Vesicle-based microfluidic measurements of interfacial rheology could be especially useful to evaluate the behavior of smart and functional polymer vesicles.[32–34] In particular, the controlled, high-throughput measurements that are achieved utilizing microfluidic technology would be ideal for biomedical and drug-design applications.

6. Conclusions

In summary, the circulation velocities and in turn the dilational and shear interfacial properties were found to be continuous functions of the interfacial composition and age of aqueous ethylene glycol droplets in a silicone oil continuous phase with surfactant. Both interfacial dilational and shear properties can be measured on small droplets typical of those employed in many applications. The diblock copolymer surfactant yields a higher viscosity interface than does the small-molecule surfactant (butanol). Both surfactant-stabilized interfaces exhibit Marangoni forces and therefore suppress dilation deformation much more than shear. A new Marangoni-induced stagnation point is also identified theoretically and observed experimentally. Even weak elasticity associated with a surface-active impurity can significantly suppress dilation. We anticipate that increased availability of such shear and dilational interfacial rheological properties will lead to improved rules of thumb for emulsion preparation, stabilization, and general practice.

Acknowledgments

Financial support for K.A.E., J.D.M. and J.T.S. was provided by the National Research Council Research Associateship Program.

Appendix A. Sensitivity of velocities to errors in measurement position

In this section, we will determine the sensitivity of the velocity at a point on and within the droplet to errors in the location of measurement (x, y, z) or of the position of the droplet (y_0) off the centerline of the flow. Given the full analytical solution for the fluid velocity [13], we evaluate the Taylor series expansion of the

velocity around a point. For example, at the center of the droplet, the sensitivity of the x -component of the velocity, $\delta v_x(C)$, is given by

$$\delta v_x(C) = \frac{\partial v_x}{\partial y} \Big|_c y + \frac{\partial v_x}{\partial z} \Big|_c z + \frac{\partial v_x}{\partial y_0} \Big|_c y_0 + \frac{\partial v_x}{\partial x} \Big|_c x + \dots \quad (8)$$

Similar expressions for the uncertainty at points A and B can be found and are not given here. We have scaled the problem using the radius of the droplet as the characteristic length. Inserting the expressions for the x -component of the velocity at positions A, B, and C gives

$$\delta v_x(A) = \frac{2}{3} \left(\frac{7}{12Bq^d + 10Bq^s + 7\lambda + 7} - \frac{6}{2Bq^d + 3\lambda + 2} + \frac{5}{4Bq^s + \lambda + 4} \right) (z - 1), \quad (9)$$

$$\delta v_x(B) = \left[\frac{2}{3} \left(-\frac{28}{12Bq^d + 10Bq^s + 7\lambda + 7} - \frac{6}{2Bq^d + 3\lambda + 2} - \frac{5}{4Bq^s + \lambda + 4} \right) + \frac{30y_0}{6Bq^d + 4Bq^s + 5\lambda + 5} + y_0 \right] (y - 1), \quad (10)$$

$$\delta v_x(C) = \left(y_0 - \frac{15y_0}{2(5 + 6Bq^d + 4Bq^s + 5\lambda)} \right) y. \quad (11)$$

A more useful demonstration of the results from these equations which is applicable to this study is to examine the limit of large Bq^d (and small Bq^s and λ). In this limit

$$\delta v_x(A) = -(5/6)\delta z, \quad (12)$$

$$\delta v_x(B) = -(y_0 - 5/6)\delta y, \quad (13)$$

$$\delta v_x(C) = y_0\delta y. \quad (14)$$

It is interesting to note that the variations at point C are second order in deviations, but A and B are first order, implying that they are more sensitive to the measurement position. Sensitivity in the measurement of Bq^d can in turn be obtained from Eq. (3), giving

$$\delta Bq^d = \frac{1}{2v_x(C)^2} \delta v_x(C). \quad (15)$$

For large Bq^d , it is clear that $\delta Bq^d/Bq^d = \delta v_x(C)/v_x(C)$, which again points to large uncertainties when $v_x(C)$ is small.

For droplets on the centerline of the flow, the equivalence of the droplet's internal velocity at the B points of Fig. 1d was verified with experiments utilizing the block copolymer surfactant. From images that looked similar to Fig. 1e where the droplet radius, a , was equal to $(48.3 \pm 1.3) \mu\text{m}$, the average dimensionless velocity of the B points was $v_x(B) = -0.312 \pm 0.032$ at $y = +a$ and -0.277 ± 0.020 at $y = -a$. The differences in velocities at $\pm a$, together with the relationships discussed above, suggest that the displacement y_0 from the mid-plane is approximately $0.017 a$, that is, $0.8 \mu\text{m}$. This result is plausible, since it is within the depth of field ($\pm 2.0 \mu\text{m}$). That it should be smaller is also reasonable because deviations of droplet center above and below are signaled by changes in contrast at the droplet edge. Based on the velocity uncertainties, the relations here suggest that deviations in measurement position are approximately $\pm 2.0 \mu\text{m}$, comparable to the size of the tracer particles. The negative value of the velocity at points B is a consequence of being in the droplet frame of reference; the streamlines adjacent to $y \pm a$ travel more slowly than the droplet. The velocities at A and B are moreover essentially equal and opposite, consistent with nearly zero dilation, as discussed in the results section. Thus, the magnitude of the velocity at the edge of a droplet located on the centerline of the flow can be accurately measured at either the A or B points.

Appendix B. Approximation of elasticity number

To illustrate the suitability of the approximation $E \approx \Pi/\sigma$, we explore it in context of the Langmuir model, which has the following relationship between interfacial tension and interfacial concentration

$$\sigma = \sigma_0 + k_B T \Gamma_{\max} \ln(1 - \Gamma/\Gamma_{\max}) \quad (16)$$

Using the definition $E = (\partial\sigma/\partial\Gamma)\Gamma/\sigma$, we compute the following ratio,

$$\frac{\Pi/\sigma}{E} = \ln(1 - \Gamma/\Gamma_{\max})^{(1 - \Gamma_{\max}/\Gamma)}, \quad (17)$$

which equals unity at small Γ and decreases ever more sharply as Γ approaches Γ_{\max} . For example, the ratio is 0.69 and 0.25 when Γ/Γ_{\max} equals 0.5 and 0.9, respectively. This approximation therefore provides an order of magnitude estimate over much of the range of interfacial concentration. If such an estimate is adequate, this approximation is very attractive since it involves only interfacial tension measurements and does not require any knowledge of the interfacial concentration. A similar expression may be derived for the Frumkin isotherm.

Appendix C. Supplementary material

Supplementary data associated with this article can be found, in the online version, at <http://dx.doi.org/10.1016/j.jcis.2012.03.078>.

References

- [1] D.T. Wasan, J. Rheol. 23 (1979) 181.
- [2] B. Madivala, S. Vandebril, J. Fransaer, J. Vermant, Soft Matter 5 (2009) 1717.
- [3] C.F. Brooks, Rheol. Bull. 81 (2012) 11.
- [4] P. Erni, Soft Matter 7 (2011) 7586.
- [5] S. Vandebril, A. Franck, G.G. Fuller, P. Moldenaers, J. Vermant, Rheol. Acta 49 (2009) 131.
- [6] C.F. Brooks, G.G. Fuller, C.W. Frank, C.R. Robertson, Langmuir 15 (1999) 2450.
- [7] P. Dhar, Y. Cao, T.M. Fischer, J.A. Zasadzinski, Phys. Rev. Lett. 104 (2010).
- [8] M. Joly, Kolloid-Zeitschrift 89 (1939) 26.
- [9] R. Miller, R. Wüstneck, J. Krägel, G. Kretzschmar, Colloids Surfaces A: Physicochem. Eng. Aspects 111 (1996) 75.
- [10] J.T. Petkov, T.D. Gurkov, B.E. Campbell, R.P. Borwankar, Langmuir 16 (2000) 3703.
- [11] J.T. Cabral, S.D. Hudson, Lab Chip 6 (2006) 427.
- [12] J.D. Martin, S.D. Hudson, New J. Phys. 11 (2009) 115005.
- [13] J.T. Schwalbe, F.R. Phelan, P.M. Vlahovska, S.D. Hudson, Soft Matter 7 (2011) 7797.
- [14] F.G. Woodhouse, R.E. Goldstein, J. Fluid Mechanics (in press) (n.d.).
- [15] C. Vezy, G. Massiera, A. Viallat, Soft Matter 3 (2007) 844.
- [16] D.C. Duffy, J.C. McDonald, O.J.A. Schueller, G.M. Whitesides, Anal. Chem. 70 (1998) 4974.
- [17] G.M. Whitesides, E. Ostuni, S. Takayama, X. Jiang, D.E. Ingber, Ann. Rev. Biomed. Eng. 3 (2001) 335.
- [18] S.D. Hudson, J.T. Cabral, W.J. Goodrum, K.L. Beers, E.J. Amis, Appl. Phys. Lett. 87 (2005) 081905.
- [19] C.P. Shillaber, Photomicrography in Theory and Practice, New York, Wiley, 1949.
- [20] L.C. Louis, C. Martin, The Theory of the Microscope, New York, American Elsevier Pub. Co., 1966.
- [21] Z. He, C. Maldarelli, Z. Dagan, J. Colloid Interface Sci. 146 (1991) 442.
- [22] C.D. Eggleton, T.-M. Tsai, K.J. Stebe, Phys. Rev. Lett. 87 (2001) 048302.
- [23] F. Jin, R. Balasubramaniam, K. Stebe, J. Adhes. 80 (2004) 773.
- [24] H.C. Maru, D.T. Wasan, Chem. Eng. Sci. 34 (1979) 1295.
- [25] D.E. Tambe, M.M. Sharma, Adv. Colloid Interface Sci. 52 (1994) 1.
- [26] K.J. Stebe, S.-Y. Lin, C. Maldarelli, Phys. Fluids A 3 (1991) 3.
- [27] K.J. Stebe, C. Maldarelli, J. Colloid Interface Sci. 163 (1994) 177.
- [28] J. Ferri, K. Stebe, Adv. Colloid Interface Sci. 85 (2000) 61.
- [29] S.D. Hudson, A.M. Jamieson, B.E. Burkhart, J. Colloid Interface Sci. 265 (2003) 409.
- [30] J.G. Santiago, S.T. Wereley, C.D. Meinhardt, D.J. Beebe, R.J. Adrian, Exp. Fluids 25 (1998) 316.
- [31] M.J. Rust, M. Bates, X. Zhuang, Nat. Methods 3 (2006) 793.
- [32] M.H. Li, P. Keller, Soft Matter 5 (2009) 927.
- [33] J.Z. Du, R.K. O'Reilly, Soft Matter 5 (2009) 3544.
- [34] R. Rodríguez-García, M. Mell, I. López-Montero, J. Netzel, T. Hellweg, F. Monroy, Soft Matter 7 (2011) 1532.